International Journal of Heat and Mass Transfer 164 (2021) 120525

Contents lists available at ScienceDirect

International Journal of Heat and Mass Transfer

journal homepage: www.elsevier.com/locate/hmt

Buoyancy-driven melting and solidification heat transfer analysis in encapsulated phase change materials

Nithin Mallya, Sophia Haussener*

Laboratory of Renewable Energy Science and Engineering, Institute of Mechanical Engineering, École Polytechnique Fédérale de Lausanne, Switzerland

ARTICLE INFO

Article history:
Received 14 June 2020
Revised 22 September 2020
Accepted 23 September 2020

Keywords:
Latent heat storage
Melting
Solidification
Phase change material
Cylindrical encapsulation
Non-dimensional analysis
Heat transfer correlations
Nusselt number
Stefan number
Rayleigh number
Fourier number

ABSTRACT

Controlled melting and solidification in encapsulated phase change materials (PCMs) is of practical interest, for example, in latent heat storage applications. The choice of PCMs and the dynamic heat transfer characteristics during phase change - affecting the transient charging/discharging rates - are decisive for the energy and power density of the heat storage option. For example, highly conductive, high melting point (above 700 K) metal alloys have a potential advantage as a high energy and power density latent heat storage, compared to the widely used low conducting molten salt and paraffin wax. This advantage depends on the relative dominance of heat transfer modes that vary depending on the thermal properties of the PCM, shape of the encapsulation, and the load conditions, and must be quantified to warrant a fair comparison. We developed a 2D transient phase change model of encapsulated PCMs, accounting for phase change over a temperature range, volumetric expansion and contraction, and multimode heat transfer within the encapsulated PCM. The enthalpy-porosity method was used to model the phase change in a fixed grid. Validation was performed with literature data of low and high-conductivity PCM experiments (RT27 and lead). Two types of PCMs were subsequently investigated in detail: a high-conducting binary-eutectic alloy Al-12.6Si and a low-conducting commercially available RT27 paraffin wax (Rubitherm GmbH). The model was used to compare the phase change process and the strength of the various modes of heat transfer in the PCM filled cylindrical stainless-steel encapsulations in horizontal and vertical orientation with constant temperature walls. A full parameter study and non-dimensional analysis are presented for different PCMs. The results quantified the influence of boundary conditions, thermophysical properties and geometrical parameters on the phase change process and the contribution of the natural convection within the encapsulation. The non-dimensional analysis linked the melt fraction and heat transfer rates to a combination of the Fourier, Stefan, Rayleigh and Nusselt numbers. Fitting of the exponents of non-dimensional number groups to the heat transfer calculations allowed to provide general correlations for melting time, melt fraction, heat transfer rates, and characteristics of melting. Such correlations provide general understanding of the transient heat transfer in phase change media and provide engineering tools for designing, for example, a latent heat storage unit.

1. Introduction

The transient heat transfer problem of solid-liquid phase change in a homogeneous PCM is described by the non-linear Stefan problem [1,2]. It is characterized by an dynamically evolving melt interface, the state of which is interdependent with the latent heat exchanged at the interface. The shape and position of the melt interface changes the convective and conductive heat transfer in the PCM and, therefore, control the latent heat exchanged, and vice versa. The Stefan problem is encountered in a wide variety of applications such as metal casting [3], heat dissipation in electronic equipment [4], and especially in latent heat storage for balancing energy demand and reducing energy requirements in industrial processes such as aluminium smelting and glass manufacturing. Thermal energy storage has been commercially harnessed in more than 70% of the total installed capacity of concentrated solar power plants (CSPs) [5]. The PCMs commonly used in thermal energy storage since the 1800s have a low thermal conductivity. Attempts to overcome this limitation include the usage of extended surfaces [6], the use of multiple PCM or PCM mixtures [7], and the incorporation of a high-conductivity matrix element into the

* Corresponding author.
E-mail address: sophia.haussener@epfl.ch (S. Haussener).

https://doi.org/10.1016/j.ijheatmasstransfer.2020.120525

Nomenclature

English symbols

$\boldsymbol{u}$	velocity vector ($m\,s^{-1}$)
$\dot{q}$	heat flux ($W\,m^{-2}$)
A_{mush}	mushy constant ($kg\,m^{-3}\,s^{-1}$)
c_p	specific heat at constant pressure ($J\,kg^{-1}\,K^{-1}$)
g	acceleration due to gravity ($9.81\,m\,s^{-2}$)
H	height (m)
h	specific enthalpy ($J\,kg^{-1}$)
L	latent heat of melting ($J\,kg^{-1}$)
R	radius (m)
r^2	coefficient of determination
T	temperature (K)
u	horizontal velocity ($m\,s^{-1}$)
v	vertical velocity ($m\,s^{-1}$)
k	conductivity ($W\,m^{-1}\,K^{-1}$)
x	length along horizontal direction (m)
y	length along vertical direction (m)

Greek Symbols

α	thermal diffusivity ($m^2\,s^{-1}$)
β	liquid melt fraction
η	heat function ($W\,m^{-2}$)
μ	dynamic viscosity (Pa s)
ν	kinematic viscosity ($m^2\,s^{-1}$)
Ω	momentum source term ($kg\,m^{-3}\,s^{-1}$)
ϕ	thermal expansion coefficient (K^{-1})
ρ	density ($kg\,m^{-3}$)
σ	stress-strain tensor ($N\,m^{-2}$)
ε	small value (≈ 0.001)
ΔT	temperature difference ($\lvert T_w - T_m \rvert$ K)

Non-dimensional numbers

Fo_y	Fourier number $\left(\frac{k_l}{\rho_l c_{p,l}} \cdot \frac{t}{y^2}\right)$
Nu_y	Nusselt number $\left(\frac{\dot{q}}{\lvert T_w - T_m \rvert} \cdot \frac{y}{k_l}\right)$
Pr	Prandtl number $\left(\frac{c_{p,l}\mu}{k_l}\right)$
Ra_y	Rayleigh number $\left(\frac{g\phi \lvert T_w - T_m \rvert y^3}{\nu\alpha}\right)$
Ste	Stefan number $\left(\frac{c_{p,l} \lvert T_w - T_m \rvert}{L}\right)$
τ_y	Dimensionless time ($Ste \cdot Fo_y$)

Subscripts

l	liquid
min	minimum
m	melting point
ref	reference
s	solid
w	wall
x	horizontal direction
y	vertical direction

PCM [8]. Metal alloys have conductivities two orders of magnitude larger than paraffin waxes and molten salts [9], comparable energy densities, and higher melting temperatures [10]. These different characteristics result in higher charge/discharge rates, higher quality of heat stored, and larger exergetic efficiencies during discharge. Aluminium alloys like Al-12.6Si (with a large heat of fusion and high thermal conductivity) have been identified as interesting high-temperature and high conductivity candidates, and cycling tests for latent heat storage applications suggest their longevity is reasonable [11].

There are several studies reporting individually experimental and numerical investigations of high and low Prandtl number PCMs. However, there has never been a direct comparison of the two in a phase change melting/solidification process. An accurate prediction of the melt interface and the combined conductive-convective heat transfer modes is fundamental to calculate the melting/solidification rate and compare the PCMs accurately. Typically, studies neglect the variation in density during phase change and the natural convection in the melt [12–14], which results in inaccurate and unrealistic predictions. The use of analytical models or conduction-only models (that neglect natural convection within the PCMs) have been found to overestimate [15] the time taken to melt. Also, the deformation of the solid PCM due to the presence of natural convection has an important effect on the phase change rate. With the advent of computational power, the phase change models must be more accurate and allow tracking of the melt interface, predicting natural convection in the melt, predicting close-contact melting, capturing phase change over a temperature range, considering phase-dependent physical properties, and accounting for volumetric expansion and contraction. Here, we directly compare by numerical modelling a high-conducting binary-eutectic metal alloy (Al-12.6Si) and a low conducting paraffin wax (RT27, Rubitherm GmbH) during phase change in equivalent conditions (similar Stefan and Rayleigh numbers), in order to provide general operational and design guidelines for arbitrary heat storage systems.

Due to their frequent usage in thermal storage and their low melting point that allows transparent encapsulations, several low conductivity (i.e. high Prandtl number) PCMs have been studied experimentally. Early experiments with n-octadecane (Pr $\approx$ 54) in rectangular encapsulations with vertical heated side walls [16,17] used thermocouples and photographic techniques to capture the melt interface. It was observed that convection followed an initially conduction dominated regime. During the melting of another paraffin wax, n-eicosane (Pr $\approx$ 54) in a vertical cylindrical encapsulation heated on the vertical outer walls [18], photographs of the melt interface along with numerical simulations helped to quantify the effect of convection. The initially conduction dominated process showed a vertical melt interface followed by a buoyancy driven convection warping the interface from the top. The shapes observed during melting were found to resemble four regimes [19]: pure conduction, conduction-convection, pure convection, and shrinking solid. Similar effects of convection were also observed in melting experiments with very high Prandtl number PCMs like Lauric acid (Pr = 137) [20] inside a rectangular encapsulation. In contrast, the presence of natural convection was observed to slow down the solidification (and even to stop it completely in cases with higher temperatures differences) during solidification studies with n-eicosane [21] in a vertical cylindrical encapsulation with a cold pipe at the axis and a heated outer wall. In this case, the presence of a source and sink maintained a temperature difference that sustained the convection, unlike in other studies where only a heat source was present [18]. Studies exploring other encapsulation geometries include melting and solidification in spherical [22,23] and vertical cylindrical encapsulations [24] with the low conducting paraffin RT27 (Pr = 41.04) in a constant temperature water bath. The melt interface was recorded by a camera. Void formation due to density change was observed during solidification but natural convection showed negligible effects on the melt interface. During melting, the buoyancy driven convection characteristics observed in both shapes were quite similar, while the close-contact melting was strong only in the spherical encapsulation where the spherical bottom allows for a constant contact for conduction. Close-contact melting, speeding up the melting process, was observed in a similar study replicated using n-octadecane [25].

Gallium (Pr = 0.025) was one of the first high conductivity PCMs experimentally studied, enabled by its very low melting point. The first Ga studies [26,27] were conducted in rectangular encapsulations and used temperature distribution and its fluctuation as qualitative signs of natural convection during phase change. Convection cells, formed by buoyancy driven natural convection, were observed and their significant effect on the shape of the melt interface during melting was demonstrated experimentally even for such large conductivity PCMs. A transition to turbulent flow was observed only when the heat source was at the bottom of the encapsulation [26] and not when it was on the vertical side wall [27]. The effect of natural convection was also investigated during melting/solidification in tin (Pr = 0.015) [28,29], where the melt interface was located by a traversing probe method, but natural convection was negligible compared to large Pr PCMs. In a more recent thermal test [30] of lead (Pr = 0.0241) used as shielding material for radioactive materials, a rectangular steel encapsulation was heated on the vertical side wall and neutron radiography was used for non-intrusive and dynamic investigation of the melt interface. It was observed that the melt interface moved faster at the top of the encapsulation due to buoyancy induced convection. Similarly, in a study of the eutectic metal alloy Mg-51Zn (Pr = 0.012) [31] in a cylindrical encapsulation using synthetic oil as the heat transfer fluid (HTF), the melting process was dominated by conduction-convection events whereas the solidification process was dominated only by conduction. A subsequent numerical investigation into the effect of the thermal conductivity of the PCM on the charging (melting) rate found that the modelling conduction-convection mechanisms was crucial even in the case of low Pr PCMs. But it was also observed that the HTF to PCM heat transfer was limiting the charging rate in PCMs with conductivities larger than $20\,W\,m^{-1}\,K^{-1}$.

Modelling phase change is an integral part in interpreting the transient heat transfer during phase change. Analytical solutions to the Stefan problem are available only for 1D, semi-infinite cases, rarely practical cases. Finite element methods allow for modeling complex geometries and can be categorized into adaptive grid and fixed grid methods, depending on the desire to consider 'sharp' melt interfaces. Adaptive grid methods that explicitly track the melt interface are computationally expensive and are inapplicable to problems where the phase change occurs over a temperature range [32]. Among the fixed grid methods, the enthalpy-porosity method [33–36] has been successfully used to model Stefan problems with the possibility to incorporate convection and phase-dependent properties. The whole domain is reduced to a single liquid phase system using a momentum source term (see Section 2) to model the solid phase and the transition between them - the 'mushy zone' - is represented by a porous medium. The momentum source term is analogous to the pressure drop of a fluid flowing in a packed bed calculated through the Carmen-Kozeny equation [37] using the liquid melt fraction as porosity and a material-dependent, non-physical term called the Mushy constant (A_{mush}). A_{mush} can vary by up to five orders of magnitude, from $10^3\,kg\,m^{-3}\,s^{-1}$ to $10^8\,kg\,m^{-3}\,s^{-1}$ [30,38–40] and has been widely investigated for modelling phase change in PCMs. The mushy constant characterizes the large velocity change that occurs in the mushy zone between the solid region (with zero velocity) and the liquid region (with a finite velocity) during phase change. For example, during solidification, a higher value of the constant implies a sudden decrease in the fluid velocity to zero. The energy equation (see Section 2) is solved in its enthalpy formulation (that includes the latent heat) instead of temperature, resulting in the enthalpy-porosity formulation. Alternative methods have also been investigated to model the large velocity ramp during the phase change, including the use of variable viscosity [41] or the use of force balance equations to calculate the momentum source term [42]. The Mushy constant approach remains one of the simplest to implement, validate and use.

Here, we implemented the Volume of Fluid (VOF) method (a free-surface modelling technique to model immiscible fluids) along with the enthalpy-porosity method to allow for a volumetric expansion/contraction of the PCM during phase change. We used an expansion gap filled with a compressible gas at the top of the encapsulation. In addition to phase-dependent specific heat and conductivity, a phase-dependent density for the PCM was implemented that simulates the volume change.

Non-dimensional analyses can provide a more broadly applicable transient heat transfer characterisation of melting/solidification processes and guide the design of, for example, latent heat storage devices. The effect of the Rayleigh number, an indicator of convection, on the variation of the Nusselt number has been previously studied and a characteristic monotonic decrease was found in conduction-only models [27,43]. One of the earliest non-dimensional multi-mode heat transfer studies of a phase change process in a rectangular enclosure heated from a vertical side wall was reported by Jany et al. [19]. Theoretical correlations for the Nusselt number as a function of the dimensionless time for each heat transfer mode were obtained for a fictional PCM (Pr = 50) and a numerical procedure based on the quasi-steady natural convection approximation [27] was used to confirm the correlation. Similar behavior of the Nusselt number has been observed in an experimental melting study (with numerically calculated wall heat fluxes) of three high Prandtl number PCMs, n-eicosane (Pr ≈ 54) [18], $NaNO_3$ (Pr = 9) [40], and RT27 (Pr = 41.04) [22], in cylindrical encapsulations. Combinations of the Fourier, Grashof and Stefan numbers were used to obtain a correlation for the melt fraction [22,40]. However, the generalized correlations do not quantify the heat transfer in terms of the multiple regimes observed during phase change. A more generalized correlation is needed that clearly distinguishes the effect of convection and models its evolution. Here, we extend the theoretical study of the effects of the heat transfer modes during phase change on the Nusselt number for both low and high Prandtl number PCMs and discuss the effects of Rayleigh, Prandtl and Stefan numbers. We quantify the effect of convection during phase change and discuss the differences in physical phenomena observed during melting and solidification and represent them in the generalized correlations. Using our 2D melting and solidification simulations with different combinations of non-dimensional numbers, we provide heat transfer correlations for two specific low and high Prandtl number PCMs (RT27 and Al-12.6Si) and extend these correlations to more general cases made of PCM units with arbitrary thermophysical properties, designs and operational conditions.

2. Numerical model

We developed a computational model of an encapsulated PCM and implemented a transient enthalpy-porosity method to simulate the movement of the melt interface in a PCM storage unit, using the finite volume method and a commercial solver (ANSYS Fluent). The simulation setup for the vertical and horizontal orientations of the cylindrical encapsulations are shown in Fig. 1 in which the PCM was melted (charged) or solidified (discharged) with the outer walls of the encapsulation maintained at a constant temperature. The top and bottom faces were insulated in the vertical orientation set-up. To initialize the melting simulation, an air gap occupying 15% of the volume was modelled inside each storage unit. For the solidification simulation, we initialized a smaller air gap in accordance with the thermally expanded PCM. Air was assumed as an ideal gas and the pressure in the air gap was observed to not affect the simulation results and thus was initialized at 1 bar. The air gap-PCM interface was tracked using VOF method with explicit

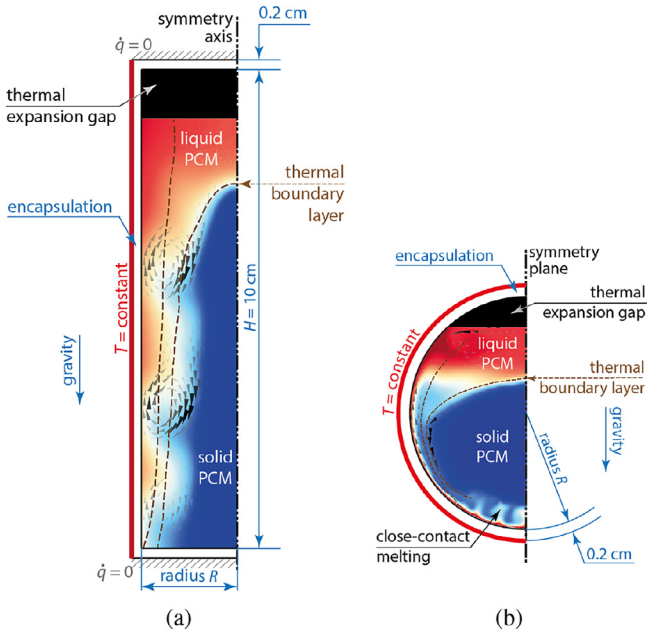

Fig. 1. (a) An axisymmetric vertical cylindrical encapsulation set-up and (b) a symmetric horizontal cylindrical encapsulation set-up, both for melting and solidification simulations. The liquid and solid phases of the PCM with schematics of the thermal boundary layers and the resulting convection cells being formed by their interaction during one of the melting simulations are shown. The thermal expansion gap, the insulated top and bottom faces for the vertical orientation, and the constant temperature outer wall condition are indicated.

formulation without any phase interactions. In VOF, each cell in the domain has a volume fraction of the air and PCM with the volume-averaged properties of the materials present in the cell. The solid PCM-molten PCM mushy interface was tracked using the enthalpy-porosity method. The PCM is considered to be in the fluid phase above the temperature T_l, in the mushy phase between T_s and T_l, and in the solid phase below T_s. In binary-eutectic alloys and pure substances (such as Al-12.6Si and RT27, respectively), the difference between T_s and T_l is very small resulting in a sharp phase change. With a temperature-range for phase change in the PCM, the liquid melt fraction, β, is defined to vary linearly with temperature:

$$\beta = \frac{T - T_s}{T_l - T_s} \tag{1}$$

with $T_s \leq T \leq T_l$. The formulation assumes a porous material behaviour in the mushy zone with the porosity equal to the liquid fraction of the cell. The mushy zone is modeled assuming a mushy fluid model [35,36] in which the solid and fluid velocities are equal in the mushy zone. This model is suitable for waxy PCMs with sharp phase change [36]. The momentum conservation equation solved in the full computational domain (incl. solid, liquid and mushy zone) is:

$$\frac{\partial}{\partial t}(\rho \boldsymbol{u}) + \nabla \cdot (\rho \boldsymbol{u}\boldsymbol{u}) = -\nabla p + \nabla \cdot \sigma + \rho g + \Omega \cdot \boldsymbol{u} \tag{2}$$

A momentum source term, Ω, mimicking the Carman-Kozeny equation for porous flow, is used in the momentum conservation Eq. (2):

$$\Omega = \frac{(1-\beta)^2}{(\beta^3 + \varepsilon)} A_{\text{mush}}. \tag{3}$$

A small value $\varepsilon \approx 0.001$ is used to prevent division by zero. In the solid phase ($\beta \to 0$), the momentum source term $\Omega = A_{\text{mush}}/\varepsilon$ and thus the value of ε is validated automatically when the mushy constant is validated to fit the experimental data. The continuity equation solved in the full domain is given by:

$$\frac{\partial \rho}{\partial t} + \nabla \cdot (\rho \boldsymbol{u}) = 0 \tag{4}$$

It was assumed that: i) the PCM is homogeneous and isotropic, ii) the flow in the molten PCM is laminar (due to the low Grashof numbers [27,44]) and a Newtonian fluid, iii) the radiative heat transfer within the encapsulation is negligible given the small temperature differences, iv) no chemical reactions take place (i.e. no formation of new compounds or intermetallics), v) no contact resistance between the encapsulation and the PCM exists, and vi) the axial flow in the horizontal orientation and angular flow in the vertical orientation of the cylindrical model that lead to changes in the Rayleigh-Bénard convection and heat transfer [45,46] are neglected. The energy conservation equation solved in the full domain is:

$$\frac{\partial}{\partial t}(\rho h) + \nabla \cdot (\rho \boldsymbol{u} h) - \nabla \cdot (k \nabla T) = 0 \tag{5}$$

where the specific enthalpy h is expressed as:

$$h = h_{\text{ref}} + \int_{T_{\text{ref}}}^{T} c_p \, dT + \beta L \tag{6}$$

L is the latent heat linearly added/removed during melting and solidification, respectively, between T_s and T_l. The assumption of a mushy fluid model [35,36] also implies convection of both sensible and latent heat in the mushy region as shown in Eq. (5).

We chose as example PCM Al-12.6Si (a high temperature, high conductivity PCM) and RT27 paraffin wax by Rubitherm GmbH (a low temperature, low conductivity PCM), given by their use as thermal storage media [11,22]. For both PCMs, cylindrical encapsulations of stainless steel (AISI 316L) with a wall thickness of 2 mm and height of 10 cm were used. Point-wise linear interpolation was used to specify the change in PCM material properties (density, specific heat capacity, and thermal conductivity) during the phase change, using the values from Table 1.

The energy, mass, and momentum conservation equations were discretized using the second order upwind scheme with a first order implicit time formulation. The SIMPLE method was used to discretize the pressure-velocity coupling in the continuity equation, and PRESTO was used to discretize the pressure correction equation. For the SIMPLE scheme to be stable, under-relaxation factors were used: 0.3 for pressure, 0.7 for momentum and 0.9 for the melt fraction. Convergence was achieved within each time step with unscaled residuals of 10^{-6} for mass, 10^{-6} for momentum and 10^{-8} for energy. Mesh size (Fig. S1) and time-step dependencies were investigated and chosen such that convergence, as well as computational efficiency, was achieved (required about 300-500 seconds per second of physical time with 10 CPUs and 40GB RAM, with some cases taking several days). Around 16000 square shaped cells were used in the rectangular shaped domain of the vertical cylinder cases with the biggest radius. Around 4000 cells were used for the largest semicircular domain of the horizontal cylinder cases.

In the presence of convection, isotherms are not an ideal way to present the results because they are only orthogonal to the direction of energy flow in the case of conductive heat transfer. Heat functions, based on enthalpy flow, are a better way of representing the convective energy flow [49]. Specific to phase change simulations, Eq. (5) at a specific point in time in 2D Cartesian coordinates can be expressed as:

$$\frac{\partial}{\partial x}\left(\rho u h - k\frac{\partial T}{\partial x}\right) + \frac{\partial}{\partial y}\left(\rho v h - k\frac{\partial T}{\partial y}\right) = 0 \tag{7}$$

The vectors for the heat function η in the x and y directions are defined as:

Table 1
Phase-dependent properties of Al-12.6Si [47,48] with $L = 470\,\mathrm{kJ\,kg^{-1}}$ and paraffin RT27 [22] with $L = 179\,\mathrm{kJ\,kg^{-1}}$.

Al-12.6Si				
Temperature T(K)	Density ρ ($\mathrm{kg\,m^{-3}}$)	Thermal Conductivity k ($\mathrm{W\,m^{-1}\,K^{-1}}$)	Specific Heat Capacity, c_p ($\mathrm{J\,kg^{-1}\,K^{-1}}$)	Viscosity μ (Pa s)
273	2700.0	160	1070	-
849 (T_s)	2587.5	160	1070	-
851 (T_l)	2460	70	1170	1.30×10^{-3}
950	2428.1	70	1170	1.30×10^{-3}
RT27				
Temperature T(K)	Density ρ ($\mathrm{kg\,m^{-3}}$)	Thermal Conductivity k ($\mathrm{W\,m^{-1}\,K^{-1}}$)	Specific Heat Capacity, c_p ($\mathrm{J\,kg^{-1}\,K^{-1}}$)	Viscosity μ (Pa s)
273	870.0	0.24	2400	-
301.15 (T_s)	870.0	0.24	2400	-
303.15 (T_l)	760.0	0.15	1800	3.24×10^{-3}
373.15	734.3	0.15	1800	3.24×10^{-3}

$$\frac{\partial \eta}{\partial y} = \frac{\partial}{\partial x}\left(\rho u h - k\frac{\partial T}{\partial x}\right) \tag{8}$$

$$\frac{\partial \eta}{\partial x} = \frac{\partial}{\partial y}\left(\rho v h - k\frac{\partial T}{\partial y}\right) \tag{9}$$

Similar to the streamlines for velocities, the net heat flow across each line with constant η is zero. Henceforth, heatlines will be used to display the heat flow through the PCM domain.

3. Results

3.1. Validation of the phase change model

Determination of the material-dependent A_{mush} requires experimental validation by melt front tracking. Such experiments are simpler for low-temperature PCMs due to the availability of transparent encapsulations that can sustain the low melting point temperatures. Tuning A_{mush} allows fitting the numerically predicted melt interface positions to the experimental data [50]. A_{mush} for the melting process of paraffin RT27 has already been fit to the experimental data [22] and suggested $A_{\mathrm{mush}} = 10^5\,\mathrm{kg\,m^{-3}\,s^{-1}}$. Independently, we performed also a numerical fit of A_{mush} to the experimental data of paraffin RT27 for the horizontally oriented cylindrical encapsulation of radius $R = 40\,\mathrm{mm}$ made of glass [22] with the outer wall maintained at $T_{\mathrm{m}} + 10\,\mathrm{K}$. Fig. 2 shows our results and the experimental data, confirming $A_{\mathrm{mush}} = 10^5\,\mathrm{kg\,m^{-3}\,s^{-1}}$ for RT27. Increasing A_{mush} pushes the natural convection region away from the melt interface, resulting in slower melting rates.

The experimental determination of the melt interface positions in high-temperature PCMs can be done either by interpolating the melt interface based on thermal maps obtained by local temperature measurements with thermocouples [26,27,31], or by imaging techniques like neutron radiography [30]. The latter provides higher precision. No such experimental phase change investigations have been reported for Al-12.6Si. Therefore, A_{mush} of Al-12.6Si ($\mathrm{Pr} = 0.0217$) was determined by using lead ($\mathrm{Pr} = 0.0241$) experiments, given the comparable properties of lead [30] and Al-12.6Si (Table 1).

Changing A_{mush} did not affect the rate of melting in the lead case, consistent with previous observations [30] and unlike for the low conductivity PCM. This is because A_{mush} only affects the convective heat transfer, which has a small influence on the melting rate in high conductivity PCMs (see Section 3.2.1). Our simulation results were always found to over-predict the melting rate by 18%, which might results from the assumed perfect insulation that differs from the experiment where heat losses on the insulated walls are still occurring in the front and back face of the encapsulation. However, A_{mush} was observed to change the physical shape of the melt interface. A lower A_{mush} implies a smaller momentum source term added to the static melting solid and, thus, a slower ramp in fluid velocity during melting. Because of this, the bottom part of the melt interface is static in the case of smaller A_{mush} (Fig. 3). Compared with the experimental results [30], the melt interface shape was well approximated with the mushy constant value of $A_{\mathrm{mush}} = 10^8\,\mathrm{kg\,m^{-3}\,s^{-1}}$. The supporting information, Fig. S2 and S3, shows the development of the melt front as a function of the chosen A_{mush} during melting and solidification in a cylindrical encapsulation of Al-12.6Si. At low A_{mush}, the momentum source term is not large enough to suppress the velocities in the solid Al-12.6Si resulting in a malleable solid and the absence of shrinkage void formation during solidification. Higher A_{mush} than $10^8\,\mathrm{kg\,m^{-3}\,s^{-1}}$ was found to not affect the melt interface.

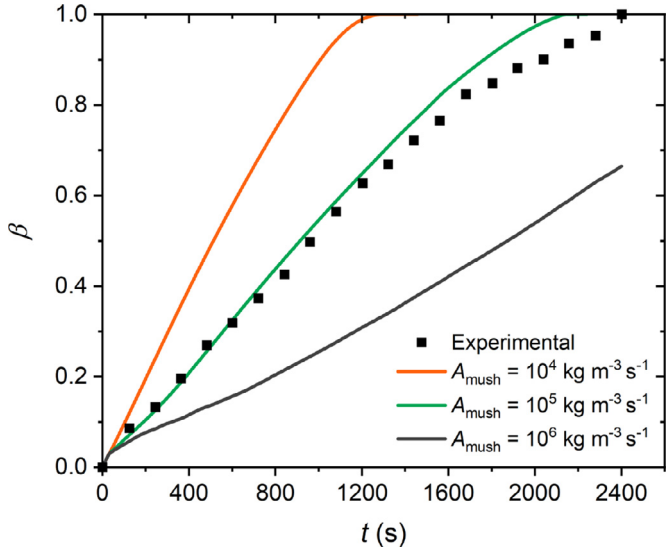

Fig. 2. Comparison of melt fraction simulated in this work and experimentally measured [22] for RT27 encapsulated in a horizontally oriented glass cylinder with $R = 40\,\mathrm{mm}$ and outer wall maintained 10 K above the T_{m}.

3.2. Non-dimensional study

In order to provide general guidelines and understanding of the heat transfer in melting/solidifying encapsulated PCMs, we use a non-dimensional analysis of the problem. We utilized Fourier, Stefan, Rayleigh, Nusselt, and Prandtl numbers. The Stefan number, Ste, is a measure of the ratio of heat stored in sensible and in latent form. The Fourier number, Fo_y, characterizes the transient heat conduction and specifically compares diffusive heat transport to the stored sensible heat. The product of Ste and Fo_y is typically

Table 2
Cases analyzed in vertical and horizontal orientations for the high and low conductivity PCMs with the corresponding non-dimensional numbers.

Case	R (cm)	H/R	Al-12.6Si, Pr = 0.0217				RT27, Pr = 41.04			
			ΔT (K)	Ste	Ra_H (x10^6) vertical	Ra_D (x10^5) horizontal	ΔT (K)	Ste	Ra_H (x10^7) vertical	Ra_D (x10^7) horizontal
1	2	5.0				0.51				
2	3	3.33	8.08	0.02	0.81	1.74				
3	4	2.5				4.14				
4	2	5.0				1.30				
5	3	3.33	20.20	0.05	2.02	4.36				
6	4	2.5				10.34				
7	2	5.0				2.59				0.63
8	3	3.33	40.40	0.10	4.04	8.72	10	0.10	9.85	2.13
9	4	2.5				20.68				5.04
10	2	5.0				5.17				1.25
11	3	3.33	80.80	0.20	8.08	17.45	20	0.20	19.51	4.21
12	4	2.5				41.36				10.00

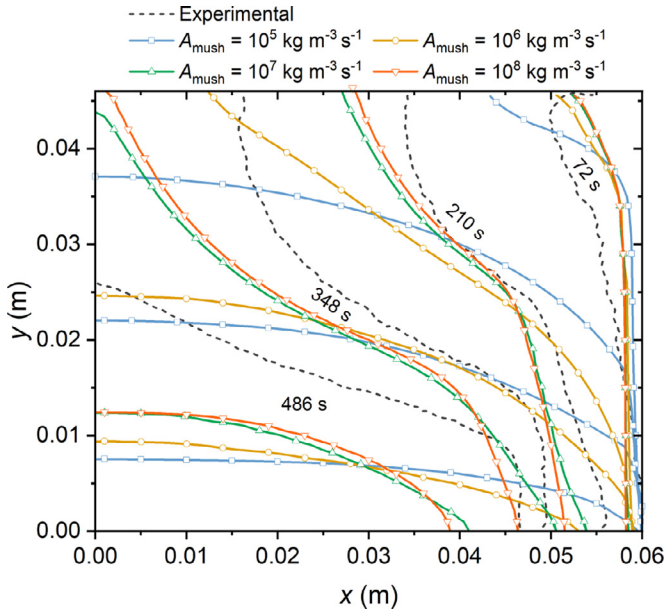

Fig. 3. Experimental [30] and simulated melt interface positions for lead in a rectangular encapsulation of size 60 mm × 50 mm and 50 mm thick with a heat flux of 35.1 kW m^{-2} applied to the right, vertical side wall.

used in phase change processes to describe a dimensionless time, τ_y. The Rayleigh number, Ra_y, compares the time scale for conduction and convection, i.e. the ratio of viscous and buoyant forces. The Nusselt number, Nu_y, is a measure of the instantaneous heat transfer rate expressed as ratio between total and conductive heat transfer. The characteristic length of the non-dimensional numbers, y, is the height, H, in a vertical configuration, and the diameter, D, in a horizontal configuration, because the thermal boundary layers forming during phase change are along the vertical dimension of the setup (see Fig. 1). Pr is the only geometry independent non-dimensional number, a ratio of momentum to thermal diffusivity, and will be used to distinguish the PCMs (Pr = 41.04 for RT27 and Pr = 0.0217 for Al-12.6Si). The set of cases analysed for the parametric study are summarized in Table 2. To investigate the effect of a change in the wall temperature ($\Delta T = |T_w - T_m|$), Ste was varied by one order of magnitude. H was kept constant at 10 cm, while the ratio H/R varied between 2.5 and 5. R was varied while keeping Ste constant to observe the effect of Ra_y (varied by one and two orders of magnitude in the vertical and horizontal orientations, respectively). To compare the low and high conductivity PCMs, Ste were kept the same in the different cases by proportionally changing the ΔT. Cases 1–6 were not investigated for RT27 because of the small temperature differences and, consequently, large simulation times. Scale analysis was also used to compare the magnitudes of the different terms in the Navier-Stokes equations and predict their influence on the observed physics during phase change. In order to simplify the following scale analysis, it was assumed that the thermally varying properties of the PCMs are constant with only the liquid phase properties used and the 2D Navier-Stokes equation is in the incompressible form with a Boussinesq term for buoyancy. The scaling analysis also assumes that the fraction of heat transfer used to increase the temperature of the PCM is negligible compared with the fraction used to melt the PCM, i.e. Ste is assumed to be small (which is true for the cases studied in Table 2). The non-dimensional numbers will be used interchangeably with the terms they represent such as: a larger Ste implies a larger ΔT, a larger Ra_y implies a larger characteristic length and/or a larger ΔT, and a larger Nu_y implies a larger heat transfer rate for an increase in ΔT. Due to similar magnitudes of the specific heat capacity and viscosity, the two high and low conductivity PCMs will be referred to as low and high Prandtl number PCMs, respectively.

3.2.1. Melting characteristics

Depending on the presence and strength of the heat transfer modes, the phase change process during melting can be split into four regimes [19]: i) a pure conduction regime, ii) a mixed conduction-convection regime, iii) a pure convection regime, and iv) a shrinking solid regime. Fig. 4a(i) and b(i) show the pure conduction regime, where the heat from the wall is almost entirely absorbed into the fusion enthalpy with conduction being the only mode of heat transfer due to the thin melt layer. Expressed using τ_y, the Nu_y obtained from a rearranged heat balance equation scales (scaling is denoted as ~) according to Neumann's exact solution [51]:

$$Nu_y \sim \tau_y^{-1/2} \tag{10}$$

which implies that convection at this early stage is negligible. This dependence was observed in separate pure conduction simulations, which we performed by ignoring the momentum equation and solving only for the energy equation (see black dashed line in Fig. 5). Our full CFD calculated Nu_y curve was observed to follow the pure conduction behavior at low τ_y, as shown in Fig. 5 for Al-12.6Si and RT27 in case 10. A pure conduction case results in a radially shrinking cylindrical solid PCM, resulting in a uniform heat transfer rate along the wall as observed initially in the dynamic heat transfer variation plots of Fig. 4. This conductive heat transfer within the PCM defines one extreme case and forms the baseline for the Nu_y number. In the full CFD simulations, the Nu_y deviates from the pure conduction case once the melting solid PCM shape is deformed and not comparable with the cylindrical solid PCM in

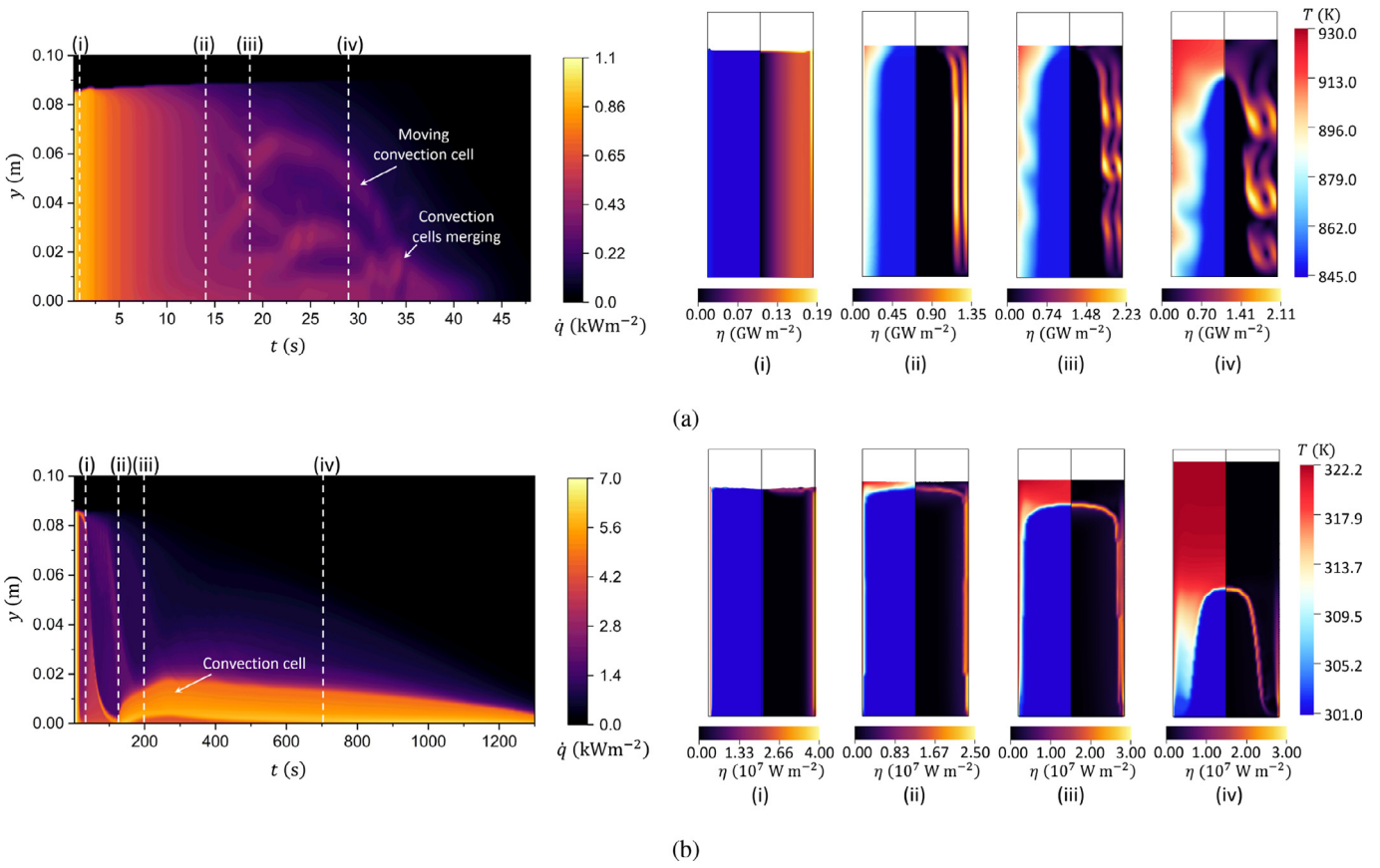

Fig. 4. Dynamic variation of multi-mode heat transfer at the heated wall for encapsulated (a) Al-12.6Si and (b) RT27 PCMs for case 10 in vertical configuration during melting. Time-dependent temperature contours and heat function vectors, η, within the melt show (i) pure conduction, (ii) mixed conduction-convection, (iii) pure convection, and (iv) shrinking solid regimes.

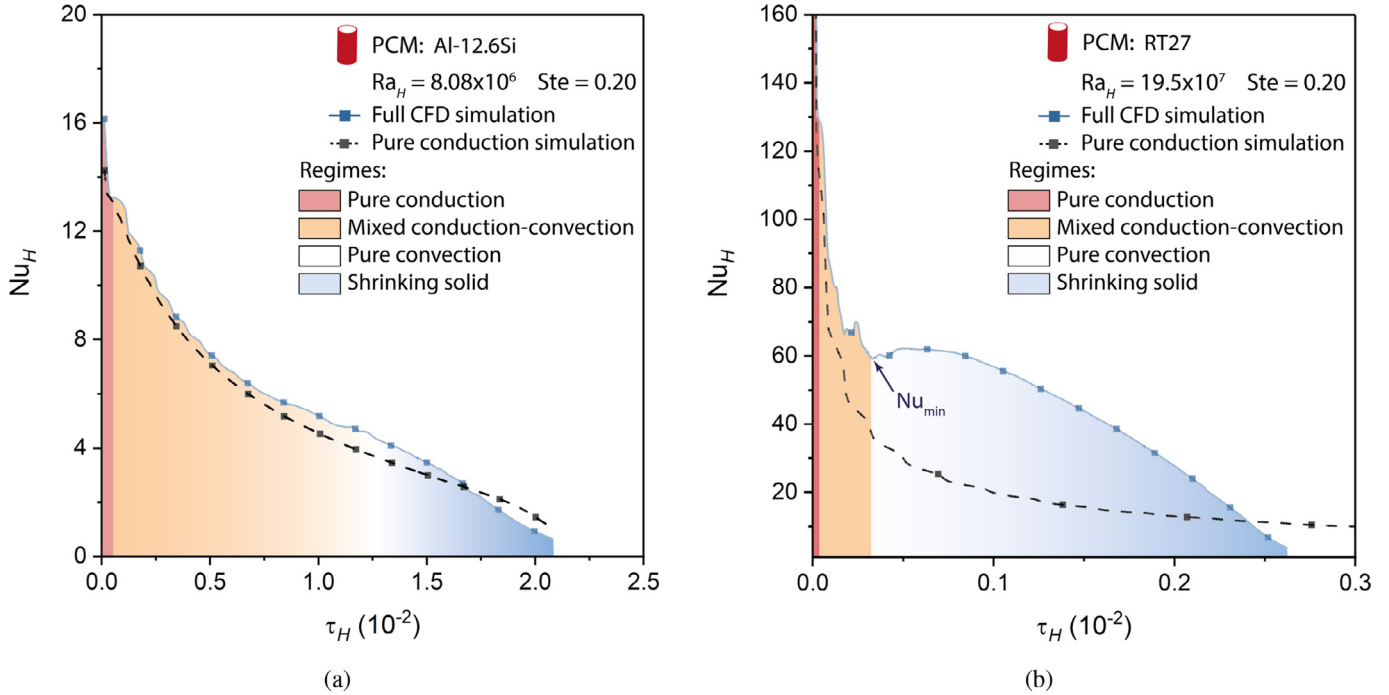

Fig. 5. Average Nu_H during melting at the heated wall as a function of τ_H for case 10 in vertical orientation for (a) Al-12.6Si and (b) RT27. The colored areas indicate the pure conduction, mixed conduction-convection, pure convection, and shrinking solid regimes.

a pure conduction case. The pure conduction simulations lags behind the full CFD simulations which results in the crossover of the Nu_y curves observed in Fig. 5. The pure conduction regime was observed to persist longer relative to the time to melt in Al-12.6Si, given by its smaller Pr. Larger initial Nu_y numbers in the pure conduction regime are observed in cases with smaller Ste and smaller Fo_y numbers.

As the melt layer thickness increases, conductive heat transfer decreases, resulting from the decreased thermal gradient and the reduced conductivity of the liquid phase of the PCMs. This allows for the two thermal boundary layers to form: one next to the hot wall and one next to the cooler melt interface as shown in Fig. 1, initiating the mixed conduction-convection regime. Conduction remains the dominant heat transfer mode in the lower section of the melt. The recirculating liquid flowing vertically up from the lower section transfers the heat from the wall to the top end of the encapsulation as observed in Fig. 4a(ii) and b(ii). In the liquid melt, the mushy source term in the momentum conservation equation is negligible because $\beta \to 1$. So the velocity of the molten fluid is obtained from the balance between the buoyancy, friction and inertia terms in the rearranged vertical momentum equation of the thermal boundary layer that scales as [19]:

$$\underbrace{\left(\frac{y}{s}\right)^4 \mathrm{Ra}_y^{-1}\mathrm{Pr}^{-1}}_{\text{Inertia}} \sim \underbrace{\left(\frac{y}{s}\right)^4 \mathrm{Ra}_y^{-1}}_{\text{Friction}} + \underbrace{1}_{\text{Buoyancy}} \tag{11}$$

For PCMs with $\mathrm{Pr} \ll 1$, the friction term is negligible due to low momentum diffusivity resulting in mass transport limited melting. For PCMs with $\mathrm{Pr} \gg 1$, the inertial term is negligible due to low thermal diffusivity resulting in thermal transport limited melting. The corresponding Nu_y is of the scale [19]:

$$\mathrm{Nu}_y \sim \begin{cases} \tau^{-1/2} + \mathrm{Ra}_y \cdot \tau^{3/2} & \text{if } \mathrm{Pr} \gg 1 \\ \tau^{-1/2} + \mathrm{Ra}_y \cdot \mathrm{Pr} \cdot \tau^{3/2} & \text{if } \mathrm{Pr} \ll 1 \end{cases} \tag{12}$$

The Nu_y curve and, effectively, the average heat transfer flux per unit temperature difference is the sum of an exponentially decreasing baseline conductive heat transfer and an Ra_y-dependent exponentially increasing convective heat transfer, which also depends on Pr for low Pr PCMs. Due to the presence of Pr in the convective heat transfer term, the effect due to convection on the net heat transfer is smaller in the case of PCMs with $\mathrm{Pr} \ll 1$, as observed comparing Al-12.6Si and RT27 (case 10 in Fig. 5). This is also the reason for the smoother and lower order of magnitude Nu_y curves of Al-12.6Si compared with RT27. In both, for a given Ste, the convective heat transfer effect scales with the Ra_y, which implies that increasing the vertical dimension of the encapsulation has a larger effect than increasing the ΔT. This is observed in the horizontal orientation simulations in Fig. 6b and d, where the diameter D is the characteristic length. For a specific Ste, Nu_y decreases according to Eq. (12) with time and reaches a local minimum:

$$\mathrm{Nu}_{y,\min} \sim \begin{cases} \mathrm{Ra}_y^{1/4} & \text{if } \mathrm{Pr} \gg 1 \\ (\mathrm{Ra}_y \cdot \mathrm{Pr})^{1/4} & \text{if } \mathrm{Pr} \ll 1 \end{cases} \tag{13}$$

The local $Nu_{y,\min}$ scales with Ra_y for a given Ste, as observed in the plots of RT27 at a given Ste (Fig. 6c and d) in which $Nu_{y,\min}$ is labeled for Case 10. The local $Nu_{y,\min}$ was lower at higher Ste because the heat flux through the wall, $\dot{q}$, did not scale proportionally with the ΔT. No specific local minimum can be observed in Fig. 6a and b for Al-12.6Si because of its low Pr.

With increasing time, decreasing conduction and increasing convection leads to the pure convection regime. The convection zone fills the entire domain and the melt interface is completely deformed (i.e. the interface shape is not parallel to the wall, see Fig. 4a(iii) and b(iii)). The thermal boundary layer thickness is proportional to:

$$\delta_y \sim \begin{cases} y \cdot \mathrm{Ra}_y^{-1/4} & \text{if } \mathrm{Pr} \gg 1 \\ y \cdot (\mathrm{Ra}_y \cdot \mathrm{Pr})^{-1/4} & \text{if } \mathrm{Pr} \ll 1 \end{cases} \tag{14}$$

The thermal boundary layers are, therefore, thicker in the high conductivity PCM case. Kelvin-Helmholtz instability convection cells are formed due to the shearing flows of the thermal boundaries next to the wall and the melting solid. Nu_y in the pure convection regime follows the same scale as $Nu_{y,\min}$, according to the boundary layer convection scaling law [52]. The effect of Ste on Nu_y was much weaker in the case of high-conductivity PCM due to its higher thermal diffusivity.

After the melting front reaches the symmetry axis, the solid PCM shrinks also along the vertical axis. The vertical size of the solid PCM determines the size of the thermal boundary layer next to the melt interface, limiting the heat transfer rate and resulting in a steep decrease of Nu_y (see Fig. 6 at large τ_y). The crossovers observed between the Nu_y curves of different Ste and Ra_y during melting in Fig. 6 imply that the cases with sufficiently higher Nu_y melt faster and finish at an earlier τ_y. The Nusselt number in this regime has been found [19] to scale as:

$$\mathrm{Nu}_y \sim \begin{cases} \left[1 - \mathrm{Ra}_y^{1/4}(\tau_y - \frac{R}{y}\mathrm{Ra}_y^{-1/4})\right]^{3/5} & \text{if } \mathrm{Pr} \gg 1 \\ \left[1 - \mathrm{Ra}_y^{1/4}(\tau_y - \frac{R}{y}(\mathrm{Ra}_y \cdot \mathrm{Pr})^{-1/4})\right]^{3/5} & \text{if } \mathrm{Pr} \ll 1 \end{cases} \tag{15}$$

which indicates a steeper descent of the Nusselt number at higher Ra_y values.

In the high Pr_y PCM, the melting time in the vertical orientation was observed to decrease by a factor of 5 in the case 10 when convection was simulated. For the horizontal orientation, we observed the melting time to decrease due to convection by a factor of 10 for case 10 (high Ste), due to the presence of close contact melting unlike the vertical orientation, and by a factor of 16 times for case 7 (low Ste). In contrast, for case 10 in the low Pr_y PCM, we observe only an decrease in melting time by a factor of 1.07 and 1.22 for the vertical and horizontal orientations, respectively, which clearly illustrates the importance of modeling convection in high Pr_y PCMs.

3.2.2. Solidification characteristics

The variation of the average Nu_H during solidification in a vertical cylinder configuration for Al-12.6Si and RT27 are shown in Fig. 7. Even though convection was observed in the molten PCM, the layer of solidifying PCM between the cool wall and molten PCM forces the heat transfer to be limited by conduction. Only a single thermal boundary layer - next to the solidified PCM - is present in the solidification case. A single convection cell spanning the length of the melt interface is observed during solidification. This is different compared to melting where multiple convection cells were formed as the two thermal boundary layers interact. Conductivity of the solid PCM is lower than the conductivity of the liquid PCM for Al-12.6Si and RT27. Thus the entire liquid PCM (its temperature already close the melting point) experiences a very small thermal gradient resulting in lower convection velocities (one magnitude lower than during melting) and negligible convection effects, that further decrease with time. This is confirmed when comparing the results with a pure conduction simulation (simulated by ignoring the momentum equation and solving only the energy equation) for case 10 in Al12Si (Fig. 7a), nearly

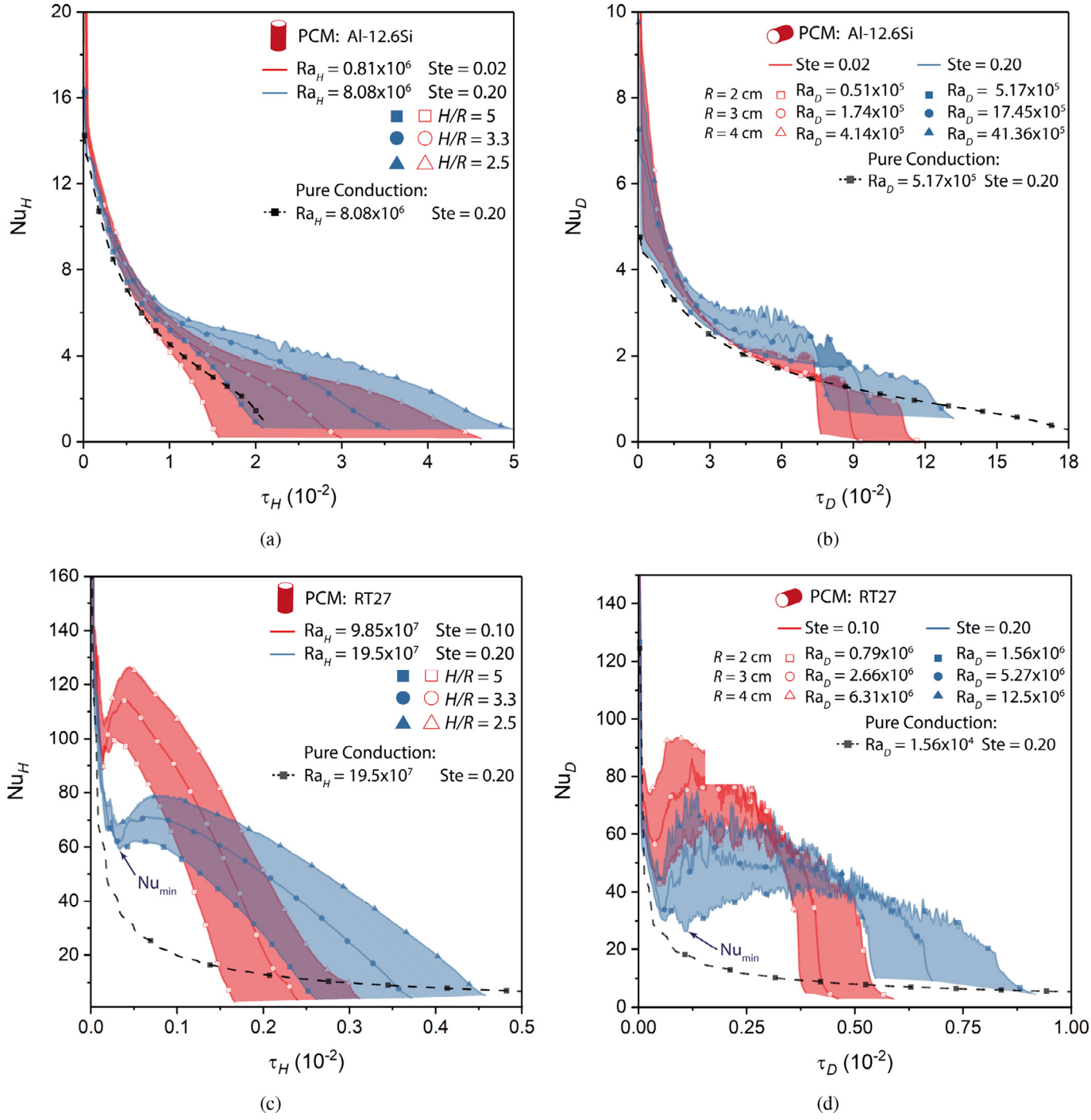

Fig. 6. Average Nu_y during melting at the heated wall as a function of τ_y in vertical and horizontal orientations for Al-12.6Si (a and b) and RT27 (c and d). $Nu_{y,min}$ is indicated for Case 10 of RT27 for both orientations.

overlapping with the simulation including convection (root mean square error of 0.091). In the pure conduction regime, Nu_H scales by Eq. (10). Convection effects are observed during the solidification of RT27 (Fig. 7b) but the exponential decrease of the Nu_H indicate a conduction dominated heat transfer. The simulation without convection for case 10 was found to underestimate the melting time by a factor of 1.3 for the high Pr_y PCM. Increased convection effects during solidification have been experimentally only observed in the presence of a hot and cold wall on either side of the solidifying PCM [21]. At the end of solidification, a phenomenon similar to the shrinking solid regime is observed due to the decreased area of melt interface for heat transfer, decreasing Nu_H.

3.2.3. Generalization

To generalize the results obtained for different PCMs, orientations and boundary conditions, relations between dimensionless groups (Nu, Fo_y, Ste, Ra_y) were identified and fitted by minimization of least mean squares. The correlations and simulated data points are shown in Fig. 8. The aspect ratio, *H/R*, was used for the generalization to include cases with different radii. The gen-

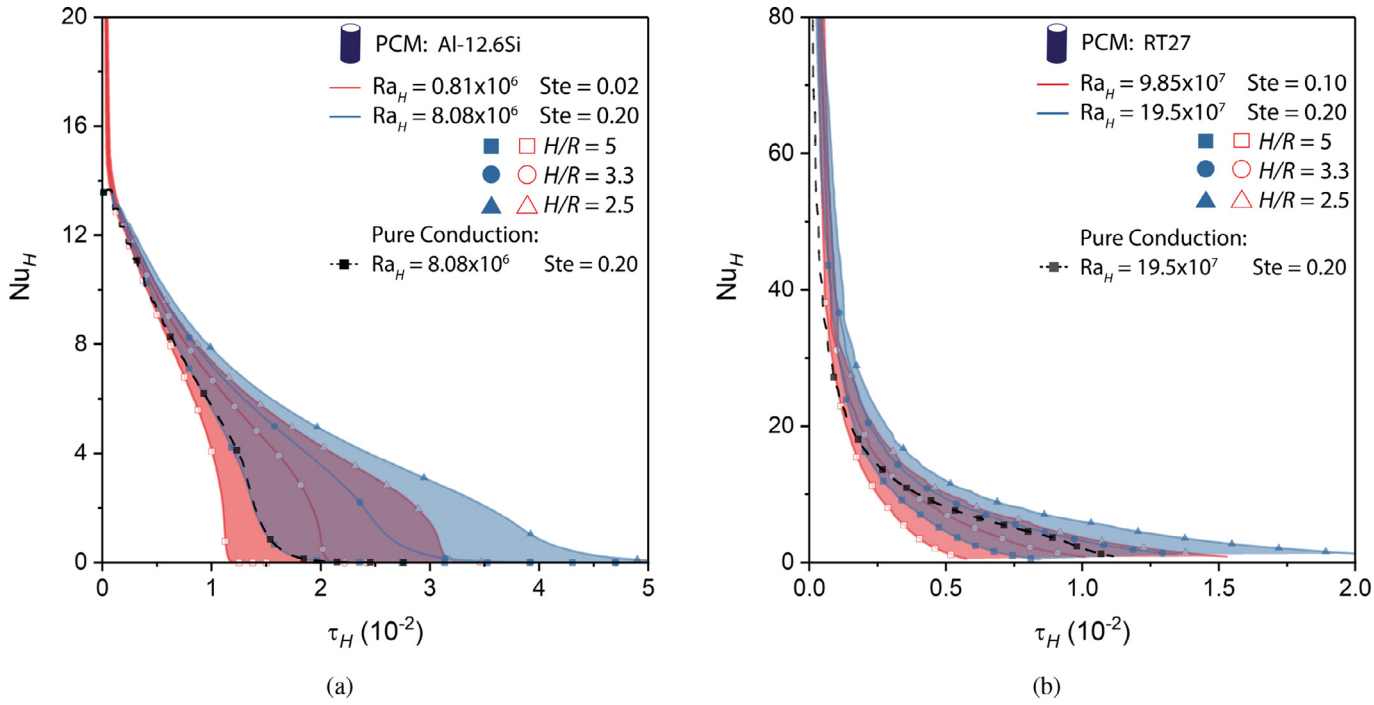

Fig. 7. Average Nu_H during solidification at the cooled wall as a function of τ_H for (a) Al-12.6Si and (b) RT27 in vertical orientation.

eralized melt fraction and heat transfer curves are of similar but distinguishable shapes depending on the type of PCM (i.e. Pr) and orientation of the encapsulation. The identified relations enable the prediction of melting time and heat transfer at the walls for cylindrical encapsulations of any material, dimension or operating condition. Because the generalizations are dependent on thermophysical properties of the PCM, the corresponding correlations can also be used to predict the loss of storage capacity of an encapsulated PCM that degrades with time (i.e. its thermal properties vary with time), for example, by the formation of intermetallic interlayers as observed in Al-12.6Si encapsulated by stainless steel [11].

Analytical correlations were formulated for the different cases with an exponential approximation for the melt fraction variation (Eq. (16), negative sign for melting and positive sign for solidification), and a combination of three Gaussian curves approximation for the non-dimensional heat transfer rate variation (Eq. (17)). The three Gaussian curves account for the exponentially varying conduction and convective terms, and the steep decrease in the shrinking solid regime.

$$\text{melt fraction} = a_0 \pm e^{-b_0 \cdot x + c_0} \tag{16}$$

$$\mathrm{Nu}_y \cdot \mathrm{Ste}^{(1-\gamma)} \cdot \mathrm{Ra}_y^{-0.25} = \underbrace{a_1 \cdot e^{-\left(\frac{x+b_1}{c_1}\right)^2}}_{\text{conduction}} + \underbrace{a_2 \cdot e^{-\left(\frac{x+b_2}{c_2}\right)^2}}_{\text{convection}} + \underbrace{a_3 \cdot e^{-\left(\frac{x+b_3}{c_3}\right)^2}}_{\text{shrinking solid}} \tag{17}$$

where $x = \mathrm{Fo}_y \cdot \mathrm{Ste}^{\gamma} \cdot \mathrm{Ra}_y^{-0.2} \cdot (H/R)^{1.4}$, and $\gamma = 0.75$ for Al-12.6Si (small Pr cases) and $\gamma = 0.25$ for RT27 (large Pr cases). The values of the coefficients for the different cases are given in the Tables 3 and 4 along with the goodness of the fit (quantified by the coefficient of determination r^2). The heat transfer due to the close contact melting in the horizontal orientations is assumed to be included in the convection term. For solidification, a similar correlation holds true, i.e. convection is present and a smaller thermal boundary layer is observed at the end of solidification due to thermal shrinkage, even though the effect of convection on the melting rate was observed to be negligible. In Eq. (17), a negative value of b_2/c_2 indicates an exponentially increasing and then decreasing convection term while a positive value indicates a decreasing convection term. The value of b_2/c_2 is positive in Al-12.6Si during both melting and solidification, indicating that the effect of convection has been decreasing since the beginning of the phase change. In RT27 during melting, the increasing-decreasing behavior of the convection term was observed due to the negative value of b_2/c_2. During solidification of RT27, a positive value of b_2/c_2 shows only the decreasing effect of convection. The generalized equations are thus capable of modeling, identifying, and separating the multiple heat transfer modes observed during the phase change. They are can aid in predicting phase change and heat transfer behavior of other PCMs with a wide range of Pr numbers.

Table 3
Coefficients of the generalized Eq. (16), describing the melt fraction in horizontal and vertical configurations for the two PCMs. r^2 goodness of the fit is also shown.

Material	Model	Coefficients			r^2
		a_0	b_0	c_0	
Al-12.6Si	Vertical Melting	1.122	0.355	0.156	0.996
	Horizontal Melting	1.322	0.209	0.293	0.996
	Vertical Solidification	−0.285	0.367	0.298	0.996
RT27	Vertical Melting	1.131	0.724	0.157	0.955
	Horizontal Melting	2.091	0.354	0.751	0.993
	Vertical Solidification	−0.014	0.650	0.0	0.959

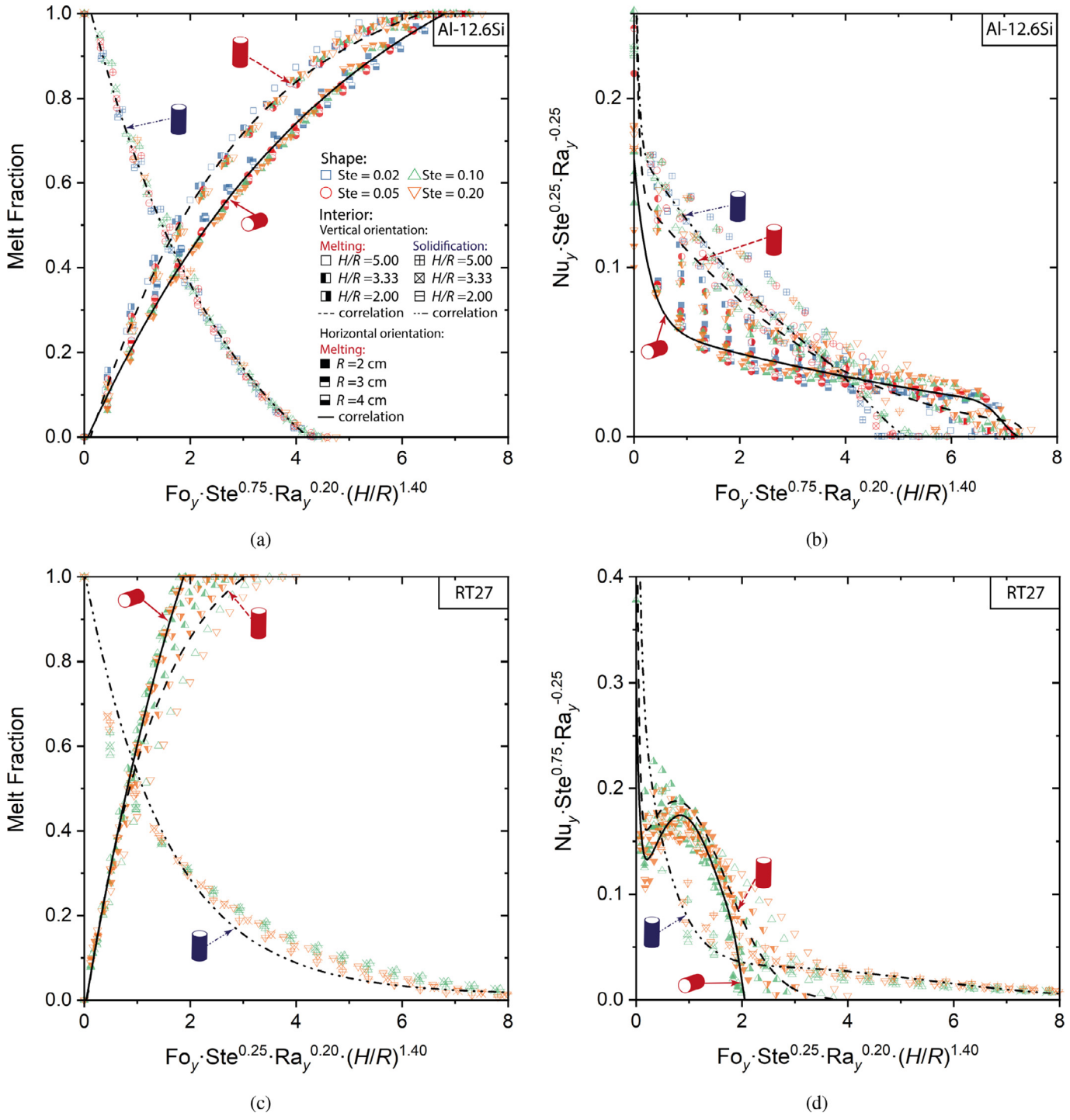

Fig. 8. Melt fraction (a and c) and non-dimensional heat transfer rate variation (b and d) for melting and solidification simulations of Al-12.6Si and for melting simulations of RT27 in vertical and horizontal orientations of the cylindrical encapsulations plotted against dimensionless time.

Table 4
Coefficients of the generalized Eq. (17), describing the heat transfer characteristics of melting and solidification in horizontal and vertical configurations for the two PCMs. r^2 goodness of the fit is also shown.

Material	Model	Coefficients									r^2
		a_1	b_1	c_1	a_2	b_2	c_2	a_3	b_3	c_3	
Al-12.6Si	Vertical Melting	4.471×10^5	1.763	0.463	0.340	6.621	7.179	−0.009	−7.514	0.188	0.889
	Horizontal Melting	1.094×10^8	11.749	2.574	0.151	12.699	13.842	−0.019	−7.326	0.508	0.845
	Vertical Solidification	2.015×10^6	2.388	0.593	0.374	5.751	6.501	−0.0224	−5.242	1.047	0.931
RT27	Vertical Melting	1.756×10^7	1.556	0.373	0.188	−0.761	1.308	−0.011	−4.01	0.179	0.878
	Horizontal Melting	2.564×10^7	2.452	0.568	0.174	−0.841	1.110	−0.061	−2.168	0.277	0.859
	Vertical Solidification	2.296×10^8	2.582	0.575	4.458	3.473	2.097	0.031	−2.387	4.346	0.9611

4. Conclusions

The heat transfer and phase change behavior in encapsulated phase change materials is of interest for heat storage and heat management applications in energy supply, medial equipment, or power electronics. A generalized and comprehensive understanding of the heat transfer modes (conduction and convection) affecting the heat transfer rates and, consequently, the power density during the phase change is essential for the design of heat storage and heat exchange applications. Melt fraction quantification and heat transfer correlations using non-dimensional numbers incorporating a large range of Prandtl numbers (i.e. a variety of different PCMs) summarize the characteristics in a compact form for various materials, different boundary conditions (i.e. load conditions), and for different designs (size, shape, or orientation). The process of phase change inside cylindrical encapsulations in horizontal and vertical orientations with a constant temperature wall was explored numerically for two distinct phase change materials (PCMs): a commercially available paraffin RT27 with low conductivity and a metal alloy Al-12.6Si with high conductivity. Enthalpy-porosity method along with the VOF method was used to model the phase change including phase-dependent properties, thermal expansion, close-contact melting, and shrink void formation during solidification. Experimental-numerical comparison of melt rate and melt interface was performed in order to fit the mushy constant, A_{mush}, a non-physical parameter of the model. Experiments with RT27 for the low conductivity PCM suggested $A_{\text{mush}} = 10^5\,\text{kg}\,\text{m}^{-3}\,\text{s}^{-1}$ and experiments with lead (a PCM with properties similar to Al-12.6Si) for the high conductivity PCM suggested $A_{\text{mush}} = 10^8\,\text{kg}\,\text{m}^{-3}\,\text{s}^{-1}$. Varying the mushy constant was observed to influence the melting rate only in low conductivity PCMs, while only the melt interface shape was affected by A_{mush} for high conductivity PCMs. This was because A_{mush} affects the convective heat transfer which has negligible contribution in high conductivity PCMs. Comparison between experiments and model also provided a validation of the model.

A parametric scaling study was then performed for a range of radii and wall temperatures. Fourier, Stefan, and Nusselt numbers were used to non-dimensionalize the results and compare the multiple cases in terms of configuration (vertical, horizontal), operating condition (wall temperature), dimension (H/R), and thermophysical properties of the PCMs (low Pr Al-12.6Si, and high Pr RT27). The phase change during melting followed different regimes (pure conduction, conduction-convection, pure convection, shrinking solid): i) in a pure conduction regime Nu_y exponentially decreases with time, ii) in a mixed conduction-convection regime, the onset of convection prevents the exponential decrease of the Nu_y, iii) in a pure convection regime, developing convection cells increase the heat transfer during melting, and iv) in a shrinking solid regime in which Nu_y decreases fast until the solid completely melts. For cylindrical encapsulations, increasing the height or vertical to horizontal aspect ratio has a larger effect on Nu_y than increasing the wall temperature. Increasing Ra_y, at a given Ste, increases the influence of convection in the melt.

It was observed that simulating convective heat transfer for phase change simulations is indispensable, especially in the case of PCMs with large Pr and Ra_y where convection dominates the heat transfer (reduction in melting time by up to 500% in vertical and 1600% in horizontal orientation). In the case of low Prandtl number PCMs, the effect of convection is less significant, given by the large conductivity of the PCM, causing change in melting time of less than 7% in vertical and 22% in the horizontal orientation. Horizontal orientations were observed to have a larger impact due to the presence of close contact melting at the bottom of the encapsulation. During solidification, convective heat transfer was absent in the low Prandtl number PCM cases as opposed to the high Prandtl number cases where simulating convection changes the solidification time by more than 30%. The effect of convection during solidification is not as crucial as during melting due to the low conducting solid layer between the cooling wall and the melt interface, forcing a conduction dominated heat transfer, similar to the pure conduction regime during melting.

Generalization of all results were presented as a combination of the non-dimensional numbers, allowing us to provide general correlations for melt fraction and normalized heat transfer ($\text{Nu}_y \cdot \text{Ste}^{(1-\gamma)} \cdot \text{Ra}_y^{-0.25}$) as a function of $\text{Fo}_y \cdot \text{Ste}^{\gamma} \cdot \text{Ra}_y^{-0.2} \cdot (H/R)^{1.4}$, with $\gamma = 0.75$ for Al-12.6Si (small Pr cases) and $\gamma = 0.25$ for RT27 (large Pr cases). The clear separation of the multi-mode heat transfer is observed with the sign of the coefficients, modeling the increasing-decreasing behavior of the buoyancy driven convection term. These correlations can be used as engineering input for the design of melting and solidification processes in encapsulated PCMs and applied in heat storage and thermal management.

Declaration of Competing Interest

None.

CRediT authorship contribution statement

Nithin Mallya: Conceptualization, Methodology, Software, Validation, Formal analysis, Writing - original draft. **Sophia Haussener:** Conceptualization, Methodology, Formal analysis, Writing - original draft, Supervision.

Acknowledgments

This material is based upon work performed in cooperation with CTI Swiss Competence Center for Energy Research (SCCER Heat and Electricity Storage).

Supplementary material

Supplementary material associated with this article can be found, in the online version, at 10.1016/j.ijheatmasstransfer.2020.120525.

References

[1] J. Stefan, Ueber die Theorie der Eisbildung, insbesondere über die Eisbildung im Polarmeere, Ann. Phys. 278 (2) (1891) 269–286, doi:10.1002/andp.18912780206.
[2] S.C. Gupta, The Classical Stefan Problem: Basic Concepts, Modelling, and Analysis, Elsevier, UK, 2003.
[3] J.M. Hill, Y.H. Wu, On a nonlinear Stefan problem arising in the continuous casting of steel, Acta Mech. 107 (1–4) (1994) 183–198, doi:10.1007/BF01201828.
[4] R. Kandasamy, X.Q. Wang, A.S. Mujumdar, Application of phase change materials in thermal management of electronics, Appl. Therm. Eng. 27 (17–18) (2007) 2822–2832, doi:10.1016/j.applthermaleng.2006.12.013.
[5] E. González-Roubaud, D. Pérez-Osorio, C. Prieto, Review of commercial thermal energy storage in concentrated solar power plants: steam vs. molten salts, Renewable and Sustainable Energy Reviews 80 (2017) 133–148, doi:10.1016/j.rser.2017.05.084.
[6] A. Pizzolato, A. Sharma, K. Maute, A. Sciacovelli, V. Verda, et al., Design of effective fins for fast PCM melting and solidification in shell-and-tube latent heat thermal energy storage through topology optimization, Applied Energy 208 (2017) 210–227, doi:10.1016/j.apenergy.2017.10.050. https://www.sciencedirect.com/science/article/pii/S0306261917314642
[7] S. Jegadheeswaran, S.D. Pohekar, Performance enhancement in latent heat thermal storage system: a review, Renewable and Sustainable Energy Reviews 13 (9) (2009) 2225–2244, doi:10.1016/J.RSER.2009.06.024. https://www.sciencedirect.com/science/article/pii/S1364032109001221
[8] W. Zhao, D.M. France, W. Yu, T. Kim, D. Singh, et al., Phase change material with graphite foam for applications in high-temperature latent heat storage systems of concentrated solar power plants, Renewable Energy 69 (2014) 134–146, doi:10.1016/j.renene.2014.03.031. http://ac.els-cdn.com/S0960148114001773/1-s2.0-S0960148114001773-main.pdf?_tid=bc3f5298-155c-11e7-a521-00000aab0f6b&acdnat=1490887549_274918de2180b25ce4b1e45753ad003b

[9] K. Cornwell, The thermal conductivity of molten salts, Journal of Physics D: Applied Physics 4 (3) (1971) 441–445, doi:10.1088/0022-3727/4/3/313. http://stacks.iop.org/0022-3727/4/i=3/a=313?key=crossref.4cd71bae0757615da5f45741883fd4bf

[10] M. Liu, N.H.S. Tay, M. Belusko, F. Bruno, et al., Investigation of cascaded shell and tube latent heat storage systems for solar tower power plants, in: Energy Procedia, vol. 69, 2015, pp. 913–924, doi:10.1016/j.egypro.2015.03.175.

[11] S. Binder, S. Haussener, Design guidelines for Al-12%Si latent heat storage encapsulations to optimize performance and mitigate degradation, Applied Surface Science (2019) 143684, doi:10.1016/j.apsusc.2019.143684. https://www.sciencedirect.com/science/article/pii/S016943321932481X

[12] L. Jian-you, Numerical and experimental investigation for heat transfer in triplex concentric tube with phase change material for thermal energy storage, Solar Energy 82 (11) (2008) 977–985, doi:10.1016/j.solener.2008.05.006.

[13] T. Rozenfeld, Y. Kozak, R. Hayat, G. Ziskind, et al., Close-contact melting in a horizontal cylindrical enclosure with longitudinal plate fins: demonstration, modeling and application to thermal storage, International Journal of Heat and Mass Transfer 86 (2015) 465–477, doi:10.1016/j.ijheatmasstransfer.2015.02.064. http://www.sciencedirect.com/science/article/pii/S0017931015002276

[14] Y.B. Tao, Y.L. He, Z.G. Qu, Numerical study on performance of molten salt phase change thermal energy storage system with enhanced tubes, Solar Energy 86 (5) (2012) 1155–1163, doi:10.1016/j.solener.2012.01.004.

[15] P. Lamberg, K. Sirén, Analytical model for melting in a semi-infinite PCM storage with an internal fin, Heat Mass Transf./Waerme- und Stoffuebertragung 39 (2) (2003) 167–176, doi:10.1007/s00231-002-0291-1.

[16] C.J. Ho, R. Viskanta, Heat transfer during melting from an isothermal vertical wall, J. Heat Transf. 106 (1) (1984) 12–19, doi:10.1115/1.3246624.

[17] C. Bénard, D. Gobin, F. Martinez, Melting in rectangular enclosures: experiments and numerical simulations, J. Heat Transf. 107 (4) (1985) 794–803, doi:10.1115/1.3247506.

[18] B.J. Jones, D. Sun, S. Krishnan, S.V. Garimella, et al., Experimental and numerical study of melting in a cylinder, Int. J. Heat Mass Transf. 49 (15–16) (2006) 2724–2738, doi:10.1016/j.ijheatmasstransfer.2006.01.006.

[19] P. Jany, A. Bejan, Scaling theory of melting with natural convection in an enclosure, Int. J. Heat Mass Transf. 31 (6) (1988) 1221–1235, doi:10.1016/0017-9310(88)90065-8.

[20] H. Shokouhmand, B. Kamkari, Experimental investigation on melting heat transfer characteristics of lauric acid in a rectangular thermal storage unit, Exp. Therm. Fluid Sci. 50 (2013) 201–222 10.1016/j.expthermflusci.2013.06.010.

[21] E.M. Sparrow, J.W. Ramsey, R.G. Kemink, Freezing Controlled by natural convection, J. Heat Transf. 101 (4) (1979) 578–584, doi:10.1115/1.3451040.

[22] E. Assis, L. Katsman, G. Ziskind, R. Letan, et al., Numerical and experimental study of melting in a spherical shell, International Journal of Heat and Mass Transfer 50 (9) (2007) 1790–1804, doi:10.1016/j.ijheatmasstransfer.2006.10.007. http://www.sciencedirect.com/science/article/pii/S0017931006005503

[23] E. Assis, G. Ziskind, R. Letan, Numerical and experimental study of solidification in a spherical shell, Journal of Heat Transfer 131 (2) (2009) 024502, doi:10.1115/1.2993543. http://heattransfer.asmedigitalcollection.asme.org/article.aspx?articleid=1475014

[24] L. Fraiman, E. Benisti, G. Ziskind, R. Letan, et al., Experimental investigation of melting in vertical circular tubes, in: ASME 2008 9th Biennial Conference on Engineering Systems Design and Analysis, 4, 2008, pp. 193–198, doi:10.1115/ESDA2008-59224. http://proceedings.asmedigitalcollection.asme.org/proceeding.aspx?articleid=1637273

[25] F.L. Tan, Constrained and unconstrained melting inside a sphere, Int. Commun. Heat Mass Transf. 35 (4) (2008) 466–475, doi:10.1016/j.icheatmasstransfer.2007.09.008.

[26] C. Gau, R. Viskanta, Effect of natural convection on solidification from above and melting from below of a pure metal, Int. J. Heat Mass Transf. 28 (3) (1985) 573–587, doi:10.1016/0017-9310(85)90180-2.

[27] C. Gau, R. Viskanta, Melting and solidification of a pure metal on a vertical wall, J. Heat Transf. 108 (1) (1986) 174–181, doi:10.1115/1.3246884.

[28] F. Wolff, R. Viskanta, Melting of a pure metal from a vertical wall, Exp. Heat Transf. 1 (1) (1987) 17–30, doi:10.1080/08916158708946328.

[29] F. Wolff, R. Viskanta, Solidification of a pure metal at a vertical wall in the presence of liquid superheat, Int. J. Heat Mass Transf. 31 (8) (1988) 1735–1744, doi:10.1016/0017-9310(88)90285-2.

[30] L. Kumar, B.S. Manjunath, R.J. Patel, S.G. Markandeya, R.G. Agrawal, A. Agrawal, Y. Kashyap, P.S. Sarkar, A. Sinha, K.N. Iyer, S.V. Prabhu, et al., Experimental investigations on melting of lead in a cuboid with constant heat flux boundary condition using thermal neutron radiography, International Journal of Thermal Sciences 61 (2012) 15–27, doi:10.1016/j.ijthermalsci.2012.06.014. https://www.sciencedirect.com/science/article/pii/S1290072912001913

[31] P. Blanco-Rodríguez, J. Rodríguez-Aseguinolaza, A. Gil, E. Risueño, B. D'Aguanno, I. Loroño, L. Martín, et al., Experiments on a lab scale TES unit using eutectic metal alloy as PCM, in: Energy Procedia, vol. 69, 2015, pp. 769–778, doi:10.1016/j.egypro.2015.03.087.

[32] Y. Dutil, D.R. Rousse, N.B. Salah, S. Lassue, L. Zalewski, et al., A review on phase-change materials: Mathematical modeling and simulations, Renewable and Sustainable Energy Reviews 15 (1) (2011) 112–130, doi:10.1016/j.rser.2010.06.011. https://www.sciencedirect.com/science/article/pii/S1364032110001589bib1025

[33] N. Shamsundar, E.M. Sparrow, Analysis of multidimensional conduction phase change via the enthalpy model, Am. Soc. Mech. Eng. (75–HT–XX) (1975) 333–340.

[34] A.D. Brent, V.R. Voller, K.J. Reid, Enthalpy-porosity technique for modeling convection-diffusion phase change: application to the melting of a pure metal, Numerical Heat Transfer 13 (3) (1988) 297–318, doi:10.1080/10407788808913615. http://www.tandfonline.com/doi/abs/10.1080/10407788808913615

[35] V.R. Voller, A.D. Brent, C. Prakash, The modelling of heat, mass and solute transport in solidification systems, Int. J. Heat Mass Transf. 32 (9) (1989) 1719–1731, doi:10.1016/0017-9310(89)90054-9.

[36] V.R. Voller, A.D. Brent, C. Prakash, Modelling the mushy region in a binary alloy, Appl. Math. Modell. 14 (6) (1990) 320–326, doi:10.1016/0307-904X(90)90084-I.

[37] P.C. Carman, Fluid flow through granular beds, Process Saf. Environ. Prot 75 (Suppl) (1997) S32–S48, doi:10.1016/s0263-8762(97)80003-2.

[38] H. Shmueli, G. Ziskind, R. Letan, Melting in a vertical cylindrical tube: Numerical investigation and comparison with experiments, International Journal of Heat and Mass Transfer 53 (19-20) (2010) 4082–4091, doi:10.1016/j.ijheatmasstransfer.2010.05.028. http://www.sciencedirect.com/science/article/pii/S001793101000270X

[39] F. Rösler, D. Brüggemann, Shell-and-tube type latent heat thermal energy storage: numerical analysis and comparison with experiments, Heat Mass Transf. 47 (8) (2011) 1027–1033, doi:10.1007/s00231-011-0866-9.

[40] A.R. Archibold, J. Gonzalez-Aguilar, M.M. Rahman, D. Yogi Goswami, M. Romero, E.K. Stefanakos, et al., The melting process of storage materials with relatively high phase change temperatures in partially filled spherical shells, Appl. Energy 116 (2014) 243–252, doi:10.1016/j.apenergy.2013.11.048.

[41] R.R. Kasibhatla, A. König-Haagen, F. Rösler, D. Brüggemann, et al., Numerical modelling of melting and settling of an encapsulated PCM using variable viscosity, Heat Mass Transf./Waerme- und Stoffuebertragung 53 (5) (2017) 1735–1744, doi:10.1007/s00231-016-1932-0.

[42] Y. Kozak, G. Ziskind, Novel enthalpy method for modeling of PCM melting accompanied by sinking of the solid phase, Int. J. Heat Mass Transf. 112 (2017) 568–586, doi:10.1016/j.ijheatmasstransfer.2017.04.088.

[43] E.M. Sparrow, S.V. Patankar, S. Ramadhyani, Analysis of melting in the presence of natural convection in the melt region, Journal of Heat Transfer 99 (November 1977) (1977) 520–526, doi:10.1115/1.3450736. http://heattransfer.asmedigitalcollection.asme.org/article.aspx?articleid=1436738

[44] L.B. Evans, R.C. Reid, E.M. Drake, Transient natural convection in a vertical cylinder, AIChE J. 14 (2) (1968) 251–259, doi:10.1002/aic.690140210.

[45] S. Grossmann, D. Lohse, Scaling in thermal convection: a unifying theory, Journal of Fluid Mechanics 407 (2000) 27–56, doi:10.1017/S0022112099007545.9909032

[46] E.P. Van Der Poel, R.J.A.M. Stevens, D. Lohse, Comparison between two-and three-dimensional Rayleigh-Bénard convection, Journal of Fluid Mechanics 736 (2013) 177–194, doi:10.1017/jfm.2013.488. 1501.01827

[47] M.M. Kenisarin, High-temperature phase change materials for thermal energy storage, Renew. Sustain. Energy Rev. 14 (2010) 955–970, doi:10.1016/j.rser.2009.11.011.

[48] C.E. Birchenall, A.F. Riechman, Heat storage in eutectic alloys, Metall. Trans. A 11 (8) (1980) 1415–1420, doi:10.1007/BF02653497.

[49] S. Kimura, A. Bejan, The "Heatline" visualization of convective heat transfer, Trans. ASME 105 (4) (1983) 916, doi:10.1115/1.3245684.

[50] A.C. Kheirabadi, D. Groulx, Simulating phase change heat transfer using COMSOL and fluent: effect of the Mushy-zone constant, Comput. Therm. Sci. 7 (2015) 427–440, doi:10.1615/ComputThermalScien.2016014279.

[51] H.S. Carslaw, J.C. Jaeger, Conduction of Heat in Solids, 2nd Edition, 1959.

[52] J.H. Lienhard, On the commonality of equations for natural convection from immersed bodies, Int. J. Heat Mass Transf. 16 (11) (1973) 2121–2123, doi:10.1016/0017-9310(73)90116-6.